Materials Advances

ROYAL SOCIETY OF CHEMISTRY

PAPER

View Article Online
View Journal | View Issue

Check for updates

Cite this: *Mater. Adv.*, 2024, 5, 4794

Impact of the sintering parameters on the microstructural and transport properties of 60 wt% $Ce_{0.8}Gd_{0.2}O_{2-\delta}$–40 wt% $FeCo_2O_4$ composites

Liudmila Fischer, *[ab] Ke Ran, [cd] Doris Sebold, [a] Patrick Behr,[a] Stefan Baumann, *[a] Joachim Mayer,[cd] Arian Nijmeijer,[b] Henny Bouwmeester, [b] Olivier Guillon [ae] and Wilhelm A. Meulenberg [ab]

The dual-phase composite 60 wt% $Ce_{0.8}Gd_{0.2}O_{2-\delta}$–40 wt% $FeCo_2O_4$ (60CGO20–FCO) is shown to be an excellent oxygen transport membrane (OTM) with sufficient stability and oxygen permeance. To achieve a mechanically and chemically stable composite material an optimised microstructure should be designed. In general, the modification of the sintering profile is a classical way of achieving microstructure optimization as well as optimization of the functional properties of ceramic materials. Moreover, optimization of the sintering program would be beneficial to minimize the increase in porosity and achieve maximum densification with minimum pore and grain growth during sintering. Thus, the chosen 60CGO20–FCO composite has been subjected to different heat treatments to determine its impact on the main morphology characteristics, such as grain size, pore size, relative density, and porosity. The dwell time was varied between 0 and 100 hours at 1200 °C and seems to have an influence on the fraction of the resulting phases, revealing the formation of a high-temperature CoO phase after 100 hours. In other samples fired for 0–50 hours at 1200 °C fluorite, spinel, and perovskite phases are prevailing. To eliminate the undesired CoO phase the cooling rate has been varied. The results reveal that the 5 hour dwell time at 1200 °C is the most suitable one for the chosen composite material, resulting in a sufficiently dense membrane with well-distributed phases, and can be further utilized for scaling up OTM production.

Received 8th December 2023, Accepted 19th April 2024

DOI: 10.1039/d3ma01095c

rsc.li/materials-advances

1. Introduction

The development of ceramic dual-phase materials for oxygen transport membranes (OTM) attracts much attention in the scientific community as mixed ionic-electronic conductors (MIEC) are very promising for gas separation[1–5] at elevated temperatures and have the potential for improving performance and reducing the cost of several industrial processes.[6,7] MIEC materials can be used for oxygen separation from mixed gases, such as air. The oxygen separation process can include exposure to flue gases containing CO_2, SO_x, dust, and steam.[8–10] Nowadays, dense dual- and multiphase composite materials with separate ionic and electronic conductors are among the most promising and efficient materials regarding stability for application in membrane reactors.[11–16] However, these material systems are quite complex and affected by many factors, such as sintering temperature and dwell time. Thus, because of the complexity of this composite system a systematic study of the microstructure-related features is required.

Rare earth doped ceria with the fluorite structure showed to be an excellent ion-conductor,[17–19] in particular for application at temperatures <850 °C.[20,21] The $Fe_xCo_{3-x}O_4$ ($0 < x < 3$) spinel system is found to be most suitable and promising for the targeted application due to its stability in aggressive atmospheres and good electronic conductivity.[22–24] The fluorite-spinel composite $Ce_{0.8}Gd_{0.2}O_{2-\delta}$–$FeCo_2O_4$ (CGO20–FCO) is a suitable example of such a material, providing a stable structure and sufficient oxygen permeability.[25–27] The presence of both phases is key to ensure good percolation, which leads to a stable oxygen flux, and sufficient performance of the composite.[14,15] This means that the concentrations of the

---

[a] Institute of Energy and Climate Research IEK-1, Forschungszentrum Jülich GmbH, 52425 Jülich, Germany. E-mail: s.baumann@fz-juelich.de

[b] Faculty of Science and Technology, Inorganic Membranes, University of Twente, 7500 AE, Enschede, The Netherlands

[c] Central Facility for Electron Microscopy GFE, RWTH Aachen University, 52074 Aachen, Germany

[d] Ernst Ruska-Centre for Microscopy and Spectroscopy with Electrons ER-C, Forschungszentrum Jülich GmbH, 52425 Jülich, Germany

[e] Jülich Aachen Research Alliance: JARA-Energy, 52425 Jülich, Germany

individual phases should be above the percolating threshold, which is generally reported as 30 vol%.[28,29] Under ideal conditions, all selected phases should stay separate and not interact during the heat treatment. However, recent studies reported the formation of an additional emerged orthorhombic phase of the $GdFeO_3$-type after phase interaction.[13,14,30–32] This phase contributes effectively to electronic conductivity.[11,14,32]

Generally, to ensure a stable and functional dual- or multiphase material for long-term gas separation processes, the quality of the connectivity and compatibility of the two phases is crucial. Hence, a defect-free membrane with optimized phase morphology should be targeted. Under real conditions, interface between particles is imperfect and can depend on different factors, such as powder particle size, synthesis and sintering parameters. The control of the microstructure *via* modification of the heat treatment plays an important role in the solid-state sintering process and defines the properties of the material, such as density, strength, and transport features.[18,33–35]

In general, a temperature range of 1100–1500 °C is used to prepare the dual- and multiphase composites for the OTM.[18,34–36] At lower temperatures, a lack of densification can be expected, and one may obtain a material with poor mechanical properties. A temperature up to 1600 °C is necessary to yield a dense functional single phase ceria membrane.[37] However, the addition of the other oxides (*i.e.* Fe_2O_3) as sintering aids can lower the sintering temperature and reach sufficient densification of the dual-phase material.[38] For the CGO20–FCO system, the optimal sintering temperature is 1200 °C. Above 1300 °C sintering temperature undesired effects on mechanical properties in the ceramic material, in particular, ceria and ceria-based composites were reported,[33,39] which in turn might affect the transport properties of the material. Grain growth is a known phenomenon in ceria-based materials at elevated temperatures.[40,41] The effect of the temperature on the CGO20–FCO composite materials is already investigated in the context of phase interaction.[34,42–45]

However, some questions related to the phase interaction as well as the morphology of the CGO20–FCO dual-phase composite are still open. When is the phase interaction completed in the CGO20–FCO composite, considering the complexity of this system? Is there an influence of the cooling rate on the phase composition? What is the dwell time requirement for the densification and pore removal processes at 1200 °C for the studied MIEC materials? To clarify all these aspects the correlation between the dwell time and phase interaction, final morphology, and permeation performance should be investigated.

The current study aims to present detailed characterization of the 60CGO20–FCO composites, including the quantification of all phase constituent volume fractions, grain and pore size, and density as well as the porosity, and reveal the relationships between the microstructure features with the applied heat treatment and cooling methods. Furthermore, comparatively little research has been conducted on the effect of the dwell time on the morphology features and the permeation performance of the CGO20–FCO composite, which will be presented here.

2. Experimental

2.1. Sample preparation

$Ce_{0.8}Gd_{0.2}O_{2-\delta}$ (CGO20) (Cerpotech, >99%, Tiller, Norway), Fe_2O_3 (Merck, 99%) and Co_3O_4 (Merck, 99%) powders used for the experiments were synthesized by the solid-state reactive sintering method (SSRS). Fe_2O_3 and Co_3O_4 were mixed in a Fe: Co 1 : 2 ratio, resulting in spinel $FeCo_2O_4$ (FCO), which was added to commercially available Gd-doped ceria. Respective amounts of powders were weighed to create $Ce_{0.8}Gd_{0.2}O_{2-\delta}$–$FeCo_2O_4$ (CGO20–FCO) compositions with wt%-ratios of 60 : 40 and 80 : 20. The powder mixtures were ball milled in polyethylene bottles over 48 h using zirconia balls on a roller bench Roller-Mill RM1 (Zoz GmbH, Germany) at a speed of 175 rpm. After drying for 48 h in ambient air at 70 °C, powder mixtures were pressed using a uniaxial press (Paul-Otto Weber GmbH, Germany) in disc-shaped membranes in a 20-mm stainless steel die and then sintered in Muffle furnace (Nabertherm GmbH, Lilienthal, Germany) at 1200 °C for different dwell times in air with a heating rate of 5 K min^{-1} as listed in Table 1. At this sintering temperature, the spinel partially reduces into a high-temperature monoxide phase with a rock salt structure. To ensure complete reoxidation of the high-temperature Co/Fe-monoxide phase to a spinel phase that is stable at operating temperatures (600–1000 °C), a slow rate of 0.5 K min^{-1} between 900 and 800 °C was implemented in the cooling step. This rate was determined by referring to.[46,47]

After the sintering step, all samples were ground to 1 mm thick discs in two steps, by applying SiC papers with different grits from P 800 to P 1200 (by WS FLEX 18C) by using ATM Saphir 550 machine (Germany). The surface of the membrane can contribute to the oxygen exchange process in an important, though more limited way. Modifying the surface by applying a catalytic layer is required to maximize surface area, participating in the process, and minimize all possible surface limitations. On both sides of the discs, a porous $La_{0.58}Sr_{0.4}Co_{0.2}Fe_{0.8}O_{3-\delta}$ (LSCF) catalytic activation layer with a thickness of 5 μm was applied using a screen-printing technique. The resulting discs were then calcined in the furnace at 1100 °C for 5 hours.

The impact of the cooling method on the microstructural properties of the 60CGO20–FCO composite sintered at 1200 °C for 100 h was performed and used heat treatment parameters are listed in Table 2.

2.2. Characterization methods

Crystal structure. The crystal structure of the materials was determined using an X-ray diffraction (XRD) diffractometer D4 ENDEAVOR (Bruker, Karlsruhe, Germany). The diffraction angle was chosen in the range of 2θ from 10° to 80°, with increments of 0.02° for 2θ and 0.75 seconds of measurement

Table 1 Selected dwell times (t, h) at 1200 °C for the studied composites

Composite	0	0.16	0.5	1	5	20	50	100
60 : 40 CGO20–FCO	√	√	√	√	√	√	√	√
80 : 20 CGO20–FCO					√			√

Table 2 Heat treatment and cooling methods of the 60CGO20–FCO composite sintered at 1200 °C

Heat treatment and cooling method	Named further
Sintered at 1200 °C for 5 h and cooled with standard 0.5 K min^{-1} between 900 and 800 °C in the furnace	5 h
Sintered at 1200 °C for 100 h and held additionally at 850 °C for 100 h then cooled in the furnace with 0.5 K min^{-1} between 900–800 °C	Slow
Sintered at 1200 °C for 100 h and cooled with standard 0.5 K min^{-1} between 900 and 800 °C in the furnace	Standard
Sintered at 1200 °C for 100 h and cooled freely in the air outside the furnace	Fast
Sintered at 1200 °C for 100 h and quenched in water	Quenching

time per step. Analysis of the measured data was performed with X'Pert HighScore (PANalytical B.V., version 3.0.5) software. Phase quantifications and associated crystal structure analyses were carried out by Rietveld refinement using the software Profex (Version 4.2.2) software. A low error R_{wp} was held $<4\%$ for all samples, which also indicates a good fitting. The errors of each fit were calculated individually and are reported in Table 3.

Microscopy. Scanning electron microscopy (SEM) and energy dispersive X-ray spectroscopy (EDS) were used to study the morphology of the prepared materials. SEM images were taken with a Zeiss Ultra 55 and a Zeiss Semini SEM 450 (Carl Zeiss NTS GmbH, German) at different magnifications. The electronic conductivity of samples was enhanced by sputter deposition of a thin platinum layer prior to the measurement.

Further image analysis-based method was conducted *via* ImageJ software on all composite samples including ~1000 grains utilizing so-called isodata threshold method,[48] which helped to estimate the average grain size of all phases as well as area fraction of pores. However, the limited number of characterized grains/pores might induce large inaccuracy in the grain size and pore size calculations.

For transmission electron microscopy (TEM) analysis, all specimens were cut from composite pellets by focused ion beam (FIB) milling using an FEI Strata 400 system with a gallium ion beam. Further thinning and cleaning was performed using an argon ion beam in a Fischione Nanomill 1040 at beam energies of 900 eV and 500 eV. TEM and energy-filtered TEM (EFTEM) imaging was performed using an FEI Tecnai F20 at 200 kV. For high-resolution high-angle annular dark-field (HAADF) imaging and energy-dispersive X-ray spectroscopy (EDS) chemical mapping an FEI Titan G2 80–200 ChemiSTEM microscope equipped with an high brightness field emission (XFEG) gun and a probe Cs corrector was used.[49]

Oxygen permeation measurements. All composite materials were subjected to oxygen permeation experiments. The experimental setup consisted of a vertical quartz glass housing, where the membrane pellets were sealed with two gold rings with an inner diameter of 13 mm. The separation of the oxygen from ambient air fed with 250 mL N min^{-1} was performed in a temperature range between 650 °C and 1000 °C. As a sweep gas argon was used with 50 mL N min^{-1} flow rate using mass flow controllers (Bronkhorst, Germany). A mass spectrometer (Omnistar, Pfeiffer Vacuum GmbH, Germany) was used to detect concentrations of oxygen and nitrogen in the permeate gas, *i.e.*, oxygen enriched argon. With the help of the measured nitrogen concentration in the argon sweep gas, air leakage through either membrane or the sealing was calculated according to

$$j_{O_2} = F_{Ar}\left(\frac{X_{O_2} - \frac{1}{4}X_{N_2}}{1 - X_{O_2} - X_{N_2}}\right)\frac{1}{A_{mem}}$$

Here F_{Ar} is argon flow rate, *i.e.*, 50 mL N min^{-1}, X_{O_2} and X_{N_2} the oxygen and nitrogen concentration in the permeate gas, respectively. The membrane area available for permeation is $A_{mem} = 1.33\ mm^2$. The factor $\frac{1}{4}$ reflects the O_2/N_2 ratio in the air feed assuming that the leak is not gas selective.

Since the oxygen partial pressure in the permeate gas is temperature dependent, the driving force for permeation is not constant during the measurement. Additionally, the sample thickness deviation after the grinding process was ±8% from the target thickness of 1 mm. Therefore, the permeance,

Table 3 Lattice parameter (*a*) and fraction (*F*) of the phases after quantification by Rietveld refinement analyses of the 60CGO–FCO composites sintered at 1200 °C

	CGO (fluorite), *Fm*3*m*		FCO (spinel), *Fd*3*m*		Co_3O_4 (spinel), *Fd*3*m*		GCFCO (perovskite), *Pnma*				CoO *Fm*3*m*
								Lattice parameter, Å			
T, h	*F*, wt%	*a* = *b* = *c*, Å	*F* wt%	*a* = *b* = *c*, Å	*F*, wt%	*a* = *b* = *c*, Å	*F*, wt%	*a*	*b*	*c*	*F*, wt%
CGO20	100.0[0]	5.424[3]	—	—	—	—	—	—	—	—	—
0	53.9[3]	5.417[1]	17.7[3]	8.286[3]	20.3[6]	8.146[0]	8.1[6]	5.336[3]	5.609[4]	7.652[6]	—
0.16	55.4[5]	5.417[3]	17.6[3]	8.297[1]	19.6[6]	8.146[3]	7.5[9]	5.333	5.606[1]	7.641[3]	—
0.5	54.5[4]	5.419[9]	17.3[6]	8.297[7]	19.6[2]	8.146[2]	8.6[3]	5.337[3]	5.609[2]	7.652[7]	—
1	53.1[3]	5.419[2]	23.1[7]	8.280[6]	15.3[3]	8.146[0]	8.5[7]	5.337[1]	5.610[2]	7.654[8]	—
5	52.1[2]	5.418[5]	22.3[1]	8.287[3]	16.6[0]	8.125[1]	9.0[3]	5.336[3]	5.608[6]	7.639[7]	—
20	53.6[3]	5.417[3]	15.7[0]	8.298[3]	22.1[2]	8.140[3]	8.5[3]	5.339[0]	5.611[5]	7.649[8]	—
50	52.3[4]	5.416[8]	18.1[6]	8.309[2]	20.0[9]	8.138[8]	9.7[5]	5.337[6]	5.612[3]	7.653[3]	—
100	54.7[3]	5.417[2]	17.1[3]	8.330[3]	17.4[7]	8.161[3]	7.9[3]	5.341[7]	5.618[5]	7.635[3]	2.8[9]

i.e., driving force normalized permeation rate, normalized to the reference thickness L_0 = 1 mm is calculated assuming Wagner's behaviour using

$$\text{Permeance} = \frac{j_{O_2}}{\ln\dfrac{p'_{O_2}}{p''_{O_2}}}\frac{L_{\text{mem}}}{L_0}$$

Here, p'_{O_2} and p''_{O_2} are the oxygen partial pressures in the retentate and permeate gas, respectively, and L_{mem} is the actual membrane thickness. The overall experimental error is assumed to be ±10%, which is well accepted in the literature.

3. Results and discussion

Based on the realization of the complex but important microstructures of dual-phase oxygen transport membranes, the standard composite 60CGO20–FCO was subjected to sintering at 1200 °C for different dwell times and further analysed to clarify the connection between the dwell time and phase interaction, morphology as well as permeation.

3.1. Microstructure analysis

60CGO20–FCO at 1200 °C for different dwell times. The resulting XRD pattern of each as-sintered sample and before heat treatment is shown in Fig. 1. The as-pressed pellet showed the presence of the three starting oxides: Fe_2O_3, Co_3O_4, and 20 mol% Gd-doped ceria.

In all sintered samples the final microstructure consists of three phases after phase interaction: a cubic fluorite structure with space group *Fm*3*m*, a donor-doped orthorhombic $GdFeO_3$ (GCFCO) perovskite structure with space group *Pnma*, and Fe/Co rich phases with a cubic spinel structure with space group *Fm*3*m*. This is in agreement with[45] since the formation of the Fe–Co spinel in CGO20–FCO composite starts at 900 °C and perovskite at 1050 °C. An exception is the 100 hours sintered pellet, where an additional CoO rock salt phase with space group *Fm*3*m* was observed, which is a result of incomplete re-oxidization during cooling. This has already been observed in earlier research.[26,46,50] The CoO phase is difficult to distinguish in the XRD patterns since they can hardly be separated from the GCFCO and Co_3O_4 patterns, however, several peaks are marked are assigned to the CoO phase in Fig. 1. Moreover, with respect to the Fe–Co oxide phase diagram,[47] a coexistence of the two spinel phases is detected in all samples: the nominal and inverse spinel. According to the Fe–Co phase diagram, which shows that the $FeCo_2O_4$ spinel is only stable in a narrow temperature range,[51] it can be concluded that Fe-rich spinel is likely the $CoFe_2O_4$ structure in the final microstructure.

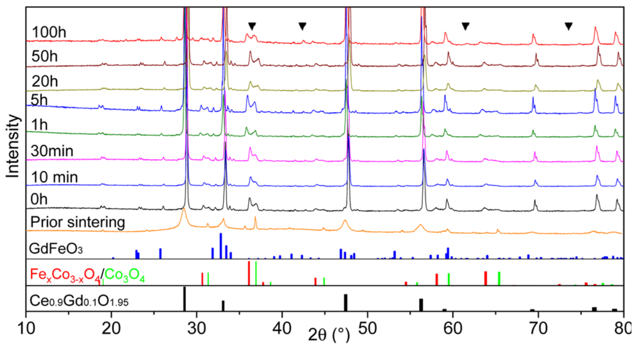

Fig. 1 The XRD patterns of the 60CGO20–FCO composite sintered at 1200 °C with various dwell times, including an unsintered pellet. CoO rock salt phase peaks are marked as a triangle. At the bottom, reference reflections are shown for the perovskite in blue, spinel in red and green, and fluorite in black.

Further Rietveld refinement quantified the composition of the dual-phase composites, which are listed Table 3. The unit-cell parameters of the pure phases are known from the literature $a_{(FeCo_2O_4)}$ = 0.8244 nm, $a_{(Fe_2CoO_4)}$ = 0.8385 nm,[24,51,52] $a_{(Co_3O_4)}$ = 0.8142 nm[52,53] and $a_{(CGO20)}$ = 0.54209 nm.[54,55] The lattice parameter of CGO20 used in our composite before phase interaction was a = 0.54246 nm and it was found to decrease by the addition of the spinel resulting in $a_{(CGO20)}$ = 0.5418 ± 0.0001 nm. It can be concluded that the fluorite phase contains 10 mol% of Gd, instead 20 mol%, due to phase interaction and formation of a GCFCO emerged phase, which is in accordance with previously published work.[11,56] There was no remarkable change in CGO lattice parameter along the whole investigated time range. The influence of the dwell time on the lattice parameter seems to be stronger for the inverse and normal spinel phases. The weight fraction of the fluorite remains almost unchanged, revealing a slightly lower amount for samples >1 hour dwell time, compared to <1 hour. The amount of GCFCO also remains almost constant in the range of 8.5 ± 1 wt%, regardless of the dwell time. The $GdFeO_3$-based perovskite phase that is formed during the sintering process can be considered as a pure electron conductor according to Ramasamy, Fischer *et al.*,[11,14] and its contribution leads to an increase in the amount of total electron conducting phase, that in turn takes place at the expense of the of ion-conducting phases. All studied samples were subjected to the analysis described in Fischer *et al.*,[57] and the resulting volume fraction of individual phases was estimated and graphically represented in Fig. 2.

The percolation threshold of 30 vol% (shown as a red dashed line in Fig. 2) has been achieved for all samples: the sum of volume fraction of all present electron conducting phases (spinels and perovskite) shown in green lays in the range of 50.5 ± 1 vol%. That explains the relatively high oxygen flux for the composites. The amount of additional CoO phase is ~2.8 vol% in a 100 hours fired sample, which likely contributes to electronic conductivity, too.[56] Due to the long dwell time the amount of CoO is increased within the composite, which in turn has not enough time for its complete reoxidation to a spinel phase.

Back scattered electron (BSE) SEM images of the surface in Fig. 3 reveal the distribution of the phases in samples fired at 1200 °C for various dwell times, including fluorite, spinel, and perovskite grains distinguished by different grey scales. It is known, that an emerging GCFCO phase appears at 1050 °C.[45]

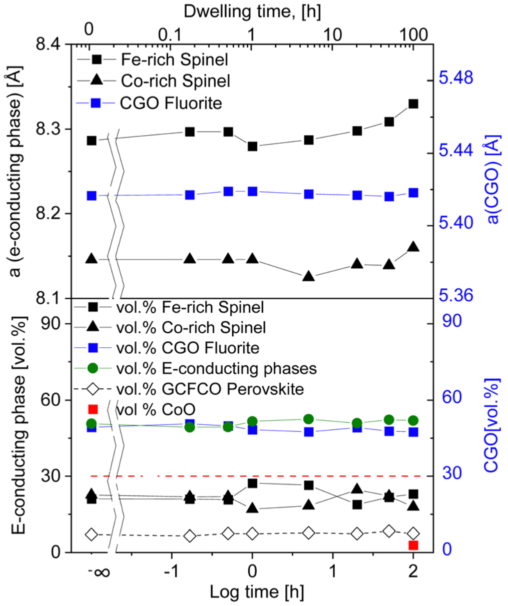

Fig. 2 Lattice parameter and volume fraction of observed phases in 60CGO20–FCO composites sintered at 1200 °C (solid lines are a guide to the eye).

In all studied samples fired at 1200 °C the perovskite phase is fully formed as indicated in light grey, dark spinel grains possess a rather uneven grain size, being coarsely distributed among white CGO grains.

Generally, there are two stages of grain growth. The initial coarsening stage is between room temperature and the sintering temperature. During this stage coarsening can be responsible for grain growth, but not a conventional boundary migration. Since the grain boundaries are possibly pinned by the open pore channels in as-pressed sample. At this stage, the density of the sample is quite low, but the particle rearrangement and surface diffusion can lead to some grain growth. After reaching the sintering temperature at the typical density above 90% the second stage of grain growth begins, where grain boundary migration *via* a diffusion process is likely to be dominating mechanism.[58] The grains grow rapidly, and pores become closed and isolated, leading also to the pore coarsening. Densification, grain, and pore growth are the three main processes that occur during sintering in the ceramic composite.[45]

Grain and pore size. The first visual analysis of the surface morphology by SEM reveals that an increase in dwell time occurring across the dwell time range of 0–1 h results in a surface with rather small grain size. Between 5–100 hours, the surface is quite plain and smooth with enlarged grains.

The grain size of each phase as well as the pore size and area fraction of pores were analysed by an image analysis-based method with ImageJ software for all samples.[48,59]

In the not single-phase composites, the uniform distribution of the one phase in the uniformly packed matrix of the second phase is required.[58] Our powder mixture consists of more than one solid prior firing process, so the grain growth is probably limited because of the second phase in the grain boundaries. Thus, in the investigated composite, the grain growth is not homogeneous and depends on the type of grains; spinel grains are slightly larger compared to the fluorite and perovskite grains.

The mean grain size of the four phases increases with increasing dwell time, as displayed in Fig. 4. Below 1 hour, the grain growth is less pronounced, with an almost constant value of 0.57 μm, followed by a gradual increase in the grain size to 0.77 μm at 50 hours. Then a drastic increase can be seen at doubling the dwell time, resulting in the largest grain size of 1.13 μm at 100 h. In general, the sintering process involves the competition of both main processes: coarsening and densification and probably depends on the dwell time at 1200 °C. It is likely that grain growth is the dominant process for the samples sintered for 50 and 100 h, while below 50 h other processes are dominant. The increased grain size in ceramic materials might lead to enhanced crack formation and poor mechanical properties.[60]

Density. Fig. 4 shows the grain and pore size, density, and porosity as a function of isothermal holding time. Three well-defined regions can be identified concerning the dominating process as a function of time. Densification is usually driven by pore agglomeration and pore-removing processes. When the

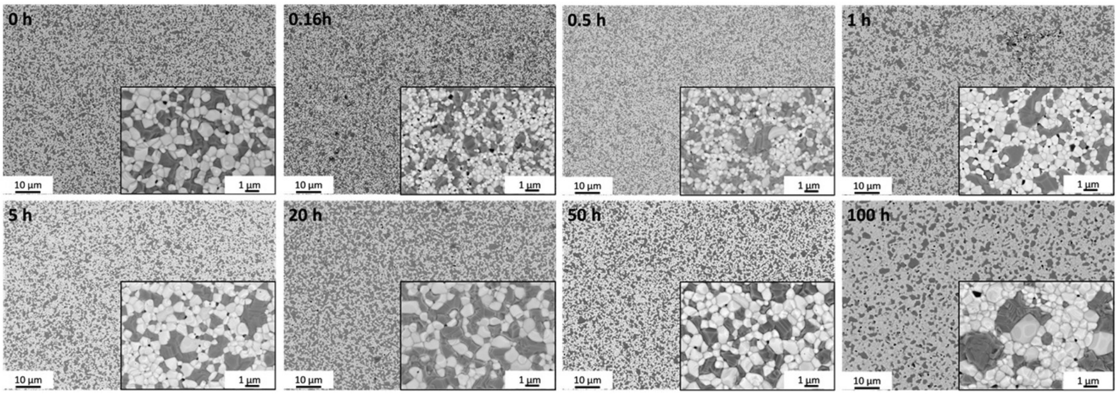

Fig. 3 BSE-images of 60CGO20–FCO surface morphology of the samples sintered at 1200 °C with two magnifications.

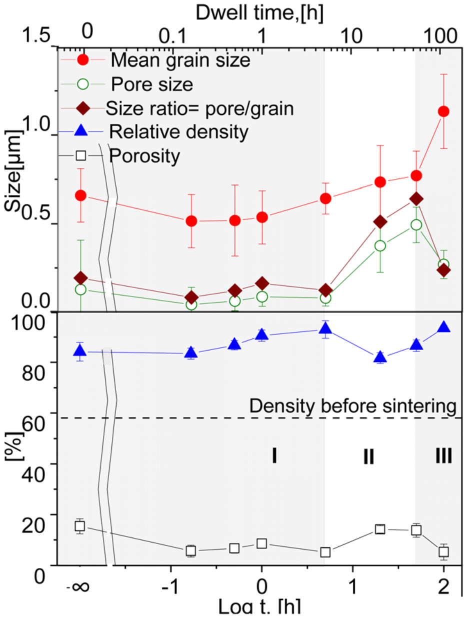

Fig. 4 Estimated relative density and porosity over the dwell time; Average grain, pore size and the pore/grain ratio dependency on the dwell time in the 60CGO20–FCO composites sintered at 1200 °C (solid lines are a guide to the eye).

grain growth is faster compared to pore growth, which naturally accompanies the grain growth, the material undergoes densification. For the analysis, the pore/grain ratio was introduced and its change describes coarsening and densification, which also helps to distinguish the regimes along the time range.[39]

An increase in density with an accompanying moderate grain growth is known for Gd-doped ceria during the first step of densification.[61] Sintering at 1200 °C for dwell times between 0 and 100 hours led to a densification level between 82 and 93% of the theoretical density. It is clear that all samples undergo some densification process already at the heating phase, as the 0 h sintered sample shows a relative density $>80\%$. In our case the samples held isothermally for less than 5 hours showed densification as the dominant process (I). The relative density of the samples gradually increases until a maximum of 93% at 5 h. Between 5 and 50 hours grain and pore growth develop concurrently with slight pore growth domination, where possibly de-densification occurs resulting in a relative density reduction (II) (similar to[42]). At 100 hours again an increase in densification is observed (III). This suggests that a sufficient dwell time for the 60CGO20–FCO composite at 1200 °C is 5 hours, where a fast and effective densification process takes place. Since the relationships between relative density and grain size are not linear, the densification processes and grain growth likely proceed *via* different diffusion routes in surface and volume, possibly due to the large difference in E_a of these diffusion mechanisms.[62]

The density of the 20 h and 50 h-fired samples rapidly decreased to a minimum (82% of the theoretical density) at 20 hours, where probably the de-densification phenomenon occurs. The observed loss in the density of the dual-phase composite could be attributed to a loss of weight as a result of oxygen gas production, with a reduction of Ce^{4+} to Ce^{3+} in the fluorite phase. In the spinel phase, the reduction of iron and cobalt also leads to a release of oxygen and the formation of a rock salt phase, which increases pore volume and size at elevated temperature.[63]

Porosity. Porosity is also affected by various dwell times, as pore growth is related to both aforementioned processes during sintering: grain growth and densification. The surface images with higher magnification in Fig. 3 display an intergranular porosity in all samples. The intragranular porosity level is relatively low for all samples, which is advantageous and gives a possibility to remove pores during the final stage of sintering for this composite. The surface image analysis is, however, incomplete since it cannot reveal distribution in the bulk, due to the "skin" layer formed on the surface. The cross-section images in Fig. 5 illustrate the dependency of the pore size and pore distribution on the dwell time in the bulk. The pore growth, migration and accumulation in connection with the dwell time are shown. There are many trapped pores along grain boundaries and in interior of the individual grains in the investigated samples. The porosity of the samples has been estimated from the SEM images *via* ImageJ software,[48] while the relative density was estimated geometrically. The resulting

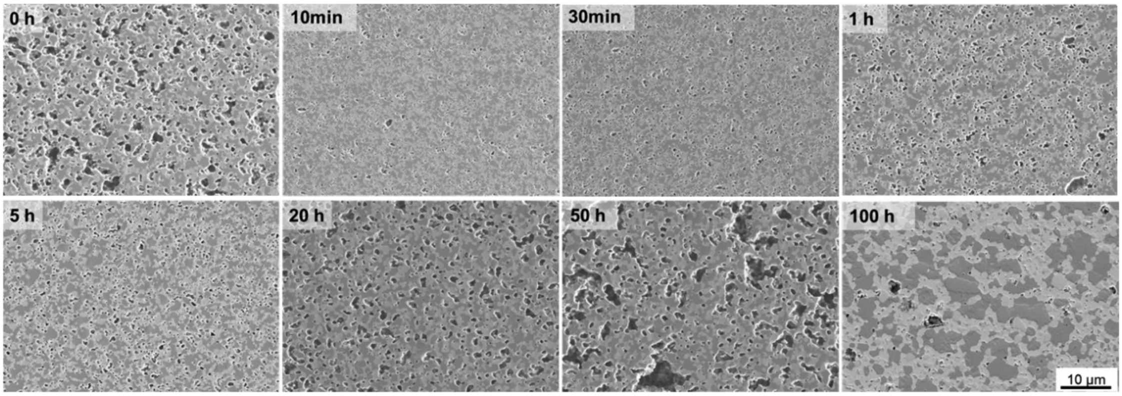

Fig. 5 SE-images of cross-section 60CGO20–FCO composite sintered at 1200 °C for different dwell time.

values are in agreement and depicted in Fig. 4. The porosity lies between 5–6% for all samples, except peaks at 0 h, 20 h, and 50 h, with 15%, 13%, and 14% respectively.

All samples fired below 5 hours exhibit a slightly higher level of open porosity with a homogeneous distribution of pores, corresponding to a densification ratio of 84–90%. Pores are also present in samples fired for >5 h, however, most of them are closed and large, which could be due to the clustering of the pores: the longer sample was held in the furnace, the more pores were united into larger ones, building a connected network. At dwell times >50 hours the pores are possibly unstable and hence both grain growth and pore removal can be observed, similar as was observed elsewhere.[39] With a dwell time below 5 hours there is no significant influence on the pore size, it remains almost constant (0.1 μm) and afterwards increases up to 0.5 μm at 50 h dwell time, followed by shrinkage of the pore size to 0.27 μm at 100 h dwell time.

Such behaviour points out that by reaching 1200 °C the process of pore clustering starts from 5 h dwell time, with simultaneous loss in material density. Based on the analysis, three main regions corresponding to the governing process can be distinguished: densification, pore-growth, and drastic grain growth, as shown in Fig. 4.

Fluorite, spinel, and orthorhombic perovskite phases are homogeneously distributed in three samples sintered for 1, 5, and 100 hours at 1200 °C as identified by TEM (EFTEM) analysis shown in Fig. 6. According to the EFTEM elemental mapping, the Fe and Co maps show a non-uniform distribution in the spinel phase, which can be subdivided into two spinel types: a normal Co-rich and an inverse Fe-rich spinel, which is in agreement with the fact that two spinel phases coexist in the composite after the phase interaction, regardless of the dwell time. The high-temperature CoO grains are seen on the elemental map of a 100 hours fired sample. Grains are mostly situated nearby the Co-rich spinel phases, while Fe-rich spinel phases are neighbours to GCFCO-like grains.

Further electron diffraction analysis performed on samples sintered for 1 and 100 hours showed the presence of three main phases in both and reveals grains of an additional phase only in the 100 hours sintered sample, as shown exemplarily in Fig. 7.

Together with the element mapping, the crystal structure fitting the best with our experimental results is the rock salt phase with the cubic structure. All observed CoO grains are contiguous to the spinel grains, namely cobalt-rich ones, and do not form any connected network for potential transport. CoO is the product of the Co_3O_4 reduction and this transformation starts already at 400 °C.[64,65] At sintering temperature (1200 °C) CoO and Co_3O_4 are in equilibrium according to the phase diagram.[47] However, below approx. 950 °C a coexistence of Co_3O_4 and FCO is thermodynamically favoured. Please note, that Co_3O_4 here refers to the crystal structure and that Fe is partly substituting Co. Since the Fe/Co-ratio in both Co_3O_4 and FCO varies with temperature, rearranging of the cations must occur during the cooling process, which obviously is not completed in this composite.[64,65]

3.2. Cooling method

Since CoO is the product of incomplete reduction of the spinel phase, some further investigation was performed to study the connection of cooling conditions with the remaining monoxide fraction. Four 100 hours sintered samples were cooled differently and analysed by XRD and Rietveld refinement. Prior to describing the results of the microstructural characterization of the 100 h sintered samples, it is important to clarify the terminology which is summarised in Table 2 in experimental section. The Slow cooling sintering program includes an additional step at 850 °C for 100 h; Fast cooling is the program, where the sample was taken out of the furnace after 100 hours sintering and cooled in ambient air, and Quenching is the sample quenched in water at room temperature after holding it for 100 hours at 1200 °C.

SEM analysis in Fig. 8 shows rather large islands of the spinel phase within the microstructure and unevenly large grains of a GCFCO emerged phase in all investigated samples sintered for 100 h with different cooling cycles. In all 100 hours fired pellets the grains are closely packed and uniformly distributed. The samples are free of cracks or any other visual defects. The difference in the phase distribution is minor for all 100 h sintered samples as well as the average grain size, which is in the range of 1.2 ± 0.1 μm for all samples.

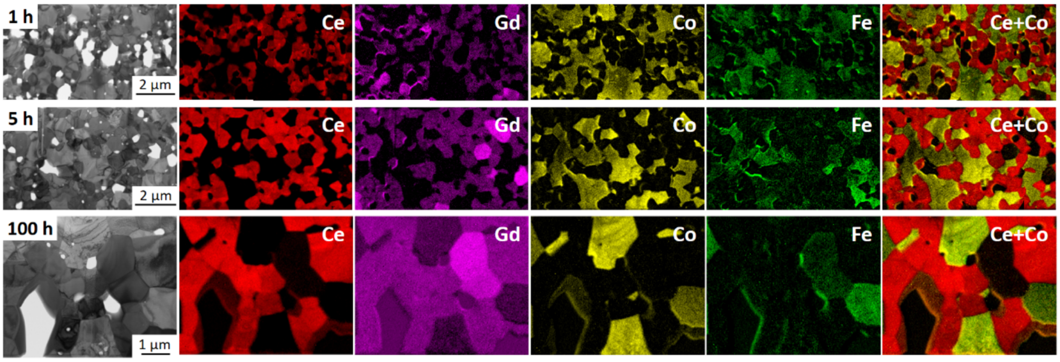

Fig. 6 Energy-filtered TEM (EFTEM) analysis of 60CGO20–FCO composite sintered at 1200 °C for 1 h, 5 h and 100 h, identifying three main phases: Gd-doped ceria (red), Fe/Co-oxide (green) and the $GdFeO_3$-based perovskite (bright magenta).

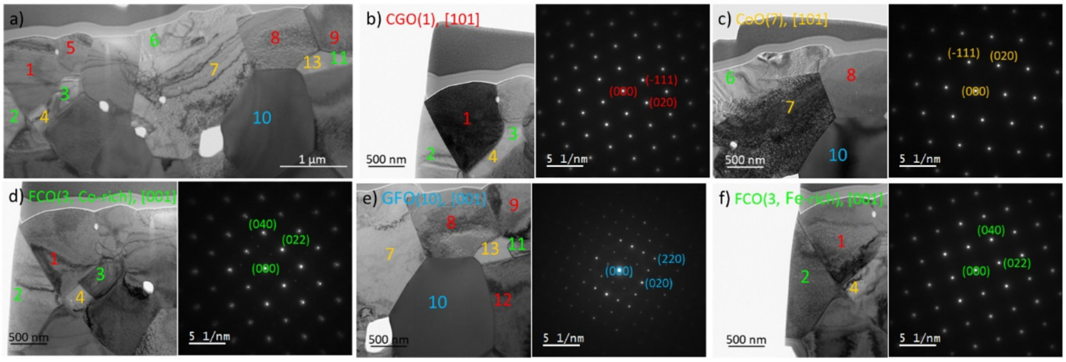

Fig. 7 Diffraction analysis of the 60CGO20–FCO composite sintered at 1200 °C for 100 h, (a) overview of investigated sample with fluorite (red), Fe/Co spinel (green), perovskite (blue) and rock salt (orange) phases, (b)–(f) individual analysis of each grain.

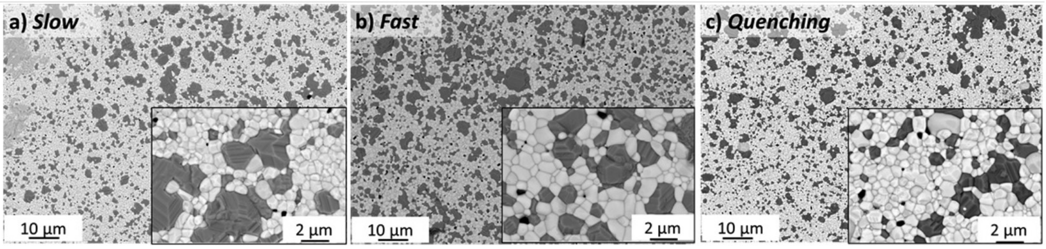

Fig. 8 BSE-images of surface morphology of 60CGO20–FCO subjected to different heat treatment in the furnace at (a) 1200 °C for 100 h and subsequent 850 °C for 100 h with standard cooling; (b) 1200 °C for 100 h with free cooling in air (c) 1200 °C for 100 h with quenching in water.

All samples sintered for 100 hours show a low level of porosity (1–5.5%) with quite small pores (0.1–0.2 µm). There is no significant influence of the cooling method on the pore size, see Fig. 9. The sample with an additional step at 850 °C for 100 h has slightly larger pores and grains, but, however, a significantly lower level of porosity (~1%) compared to other samples, resulting in a slightly improved relative density of 94.8%, while others have ~92–93%. The porosity has been estimated from the SEM images *via* image analysis, while the relative density was estimated geometrically from the dimensions and weight of the as-sintered pellets. Moreover, the limited number of characterized images might however induce inaccuracy in the porosity calculations. The character of the pores is also slightly different. All 100 h fired samples contain both types of pores intergranular and intragranular (predominantly located in the spinel phase), while the pellet with the 850 °C dwell step contains pores located along the grain boundaries. Due to slow diffusion kinetics the removal of the pores in the grain core is almost impossible, while the reduction of the pores along the grain boundary is still possible *via* grain boundary diffusion at the latter sintering stage. Hence this additional step helps to eliminate pores in the grain core and along the grain boundaries, improving the quality of the final microstructure.

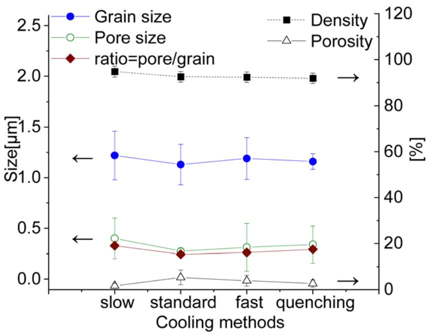

Fig. 9 Grain size, pore size, relative density and porosity of the 100 h sintered samples cooled differently (solid lines are a guide to the eye).

According to the Fe–Co–O phase diagram,[46,47] the partial reduction of the spinel into a high-temperature Co/Fe monoxide phase with a rock salt structure can occur at 1200 °C sintering temperature.[11,66] In the Co–O phase, the most thermodynamically stable phases are the cubic CoO and Co_3O_4 oxides and the transition between these two oxides is reversible.[64,65,67] A slow rate of 0.5 K min^{-1} between 900 and 800 °C was implemented in the cooling cycle to ensure its complete reoxidation to a spinel phase that is stable at target operating temperatures (600–1000 °C). Generally, this slow cooling helps the reoxidation process and Co/Fe monoxide is no more detectable (<1 wt%), as can be seen for the sample sintered for 5 hours. The resulting XRD patterns are shown in Fig. 10. The CoO peaks were observed in the 100 hours fired samples subjected to quenching, cooling in ambient air, and

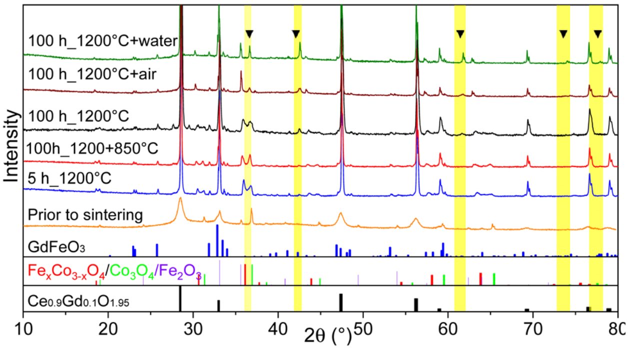

Fig. 10 XRD patterns of 60CGO20–FCO composite subjected to different heat treatment and cooling methods. At the bottom, reference reflections are shown for the perovskite in blue, spinel in red and green, and fluorite in black.

the standard cooling program. Additionally, in the Slow cooling program, Co monoxide is completely oxidized and only fluorite, spinel, and perovskite phases are present, which is almost identical to the 5 hours sintered sample. Thus, this additional step in the sintering program helps to eliminate this high-temperature CoO phase and preserve normal and inverse spinel structures.

XRD and Rietveld refinement of the surface and bulk of each sample shows a small difference in the amount of fluorite phase. In the electron-conducting phases, however, the difference is more significant across the sintered pellet. While a higher amount of GCFCO can be found in the bulk, the spinel amount is higher on the surface. The Rietveld refinement confirmed the presence of the CoO in all samples fired for 100 h, except the sample cooled slowly as depicted in Fig. 11.

In this pellet, only 0.2 vol% and 0.5 vol% of the monoxide was estimated on the surface and in the bulk, respectively, which is below the detection limit and thus will further be neglected. As expected, the maximum CoO fraction is found in the quenched sample and the fast cooled pellets, followed by the sample subjected to standard cooling in the furnace. The oxidation process of CoO on the surface and in the bulk encompasses different reactions and strongly depends on the diffusion paths.[67] The volume fraction of CoO in the bulk is higher compared to that on the surface in pellets cooled slow, standard, and fast, as shown in Fig. 11. Due to lack of diffusion time for the CoO oxidation reaction, a certain amount of CoO remains unoxidized in the bulk.

The rock salt phase itself was probably completely oxidized into Co_3O_4 during the slow cooling process, due to free access to the oxygen in the air.[46] In contrast, the quenched sample, where the oxidation process was terminated after 100 hours, contains a higher amount of the CoO on the surface, compared to that in the bulk. These results again support the theory that too drastic cooling gives no time for the reaction in the CoO–Co_3O_4 system, ending up in the high amount of 20 vol% of residual high-temperature CoO in the surface skin layer. The amount of the Co_3O_4 phase is strongly affected by heat treatment and the fraction of the rock salt: the amount of CoO increases, while Co_3O_4 decreases. Based on our observation, the rearranging of the ions happens in the cooling phase until the high-temperature phase is completely oxidized. Hence, slow cooling with an additional step is required in the sintering profile, to control the phase transformation and final morphology of the dual- or multi-phase composite. The fluorite lattice parameter remains constant independent of the cooling cycle. While the fluorite and CoO lattice parameter is almost identical for all samples in the bulk and surface, the spinel lattice parameter shows some differences, pointing out a clear trend, as shown in Fig. 12. An increase in the cooling rate leads to an increase in the lattice parameter for the iron-rich spinel and a slight increase in the cobalt-rich spinel phases, which can be attributed to the oxidation reactions upon the cooling process.[68] The larger lattice parameter indicates a higher iron content in the Fe–Co spinel phase according to Vegard's law, hence by an increase in the cooling rate an increase of the iron-rich spinel fraction in the bulk is observed with a maximum in

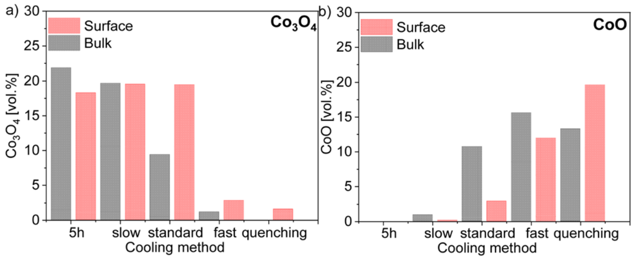

Fig. 11 Volume fraction of 60CGO20–FCO composite subjected different heat treatment and cooling methods in (a) Co_3O_4 and (b) CoO amount comparison in the bulk and surface.

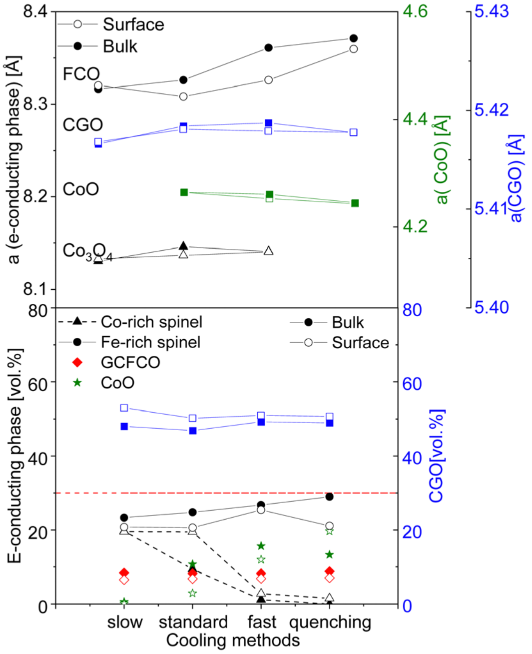

Fig. 12 Lattice parameter difference and volume fraction of spinels and CGO in the bulk and surface (solid lines are a guide to the eye).

the quenched sample. This can be explained by the difference of the cations' mobility.[69] Cobalt cations are diffusing faster so they are migrating to the surface forming CoO or/and Co_3O_4 resulting in an increase of the Co-containing phases at the surface (Fig. 12). In consequence, the Fe-containing phases (FCO and GCFCO) are more present in the bulk and increase with a faster cooling rate.

3.3. Functional properties

The temperature-dependent oxygen permeation of the composites with nominal 60CGO20–FCO sintered at 1200 °C for different times below 1 h and above 1 h are shown along with their activation energies in Fig. 13, respectively. At short dwell time (<1 hour) all Arrhenius plots of the examined composites show a kink at 880 °C indicating a change in the rate limiting process. At 1 and 5 hours, dwell time the change in activation energy is at lower temperature, *i.e.*, 800 °C, and much less pronounced. It completely disappears at longer dwell times ≥20 hours. Typically, in OTM this behaviour is ascribed to a change from bulk diffusion limitation at high temperature to surface exchange limitation at lower temperature. At high temperatures (>800 °C) the permeation rates for all examined composite membranes are almost identical with E_a in the range of 61–76 kJ mol^{-1}, which indeed can be attributed to the bulk transport, *i.e.* the ionic conductivity of the fluorite ($E_{a\,CGO20}$ = 72 kJ mol^{-1} [54,70]). The lower E_a of ∼55 kJ mol^{-1} for the 0 h sintered sample might be due to insufficient sintering and increased porosity impeding electronic conductivity. At low temperatures (650–800 °C) E_a is much higher 112–117 kJ mol^{-1} for short dwell time (<1 hour), indicating rate limitations due to surface exchange kinetics although all membranes were coated with porous LSCF activation layers on both sides.

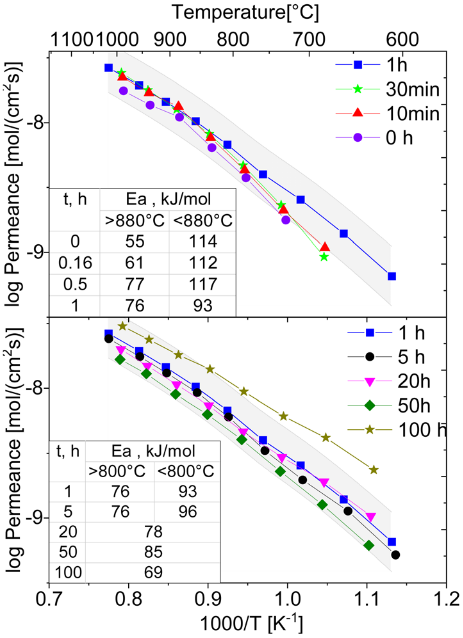

t, h	Ea , kJ/mol	
	>880°C	<880°C
0	55	114
0.16	61	112
0.5	77	117
1	76	93

t, h	Ea , kJ/mol	
	>800°C	<800°C
1	76	93
5	76	96
20	78	
50	85	
100	69	

Fig. 13 Arrhenius-type plots of oxygen flux density of the 60CGO20–FCO composite sintered at 1200 °C for 0, 1 h and 10, 30 min, 1, 5, 20, 50 and 100 hours (solid lines are a guide to the eye, grey area is ±10% error interval for the 1-hour measurement).

The resulting oxygen permeances of the coated membranes are mostly within the estimated experimental error of ±10%. Along the time range between 0 and 5 h dwell time, there is a very slight increase in permeation until 1 hour followed by a slight decrease until 50 hours dwell time. But, at 100 h dwell time a sharp increase in oxygen permeation is observed with the maximum of j_{O_2} = 0.13 mL cm^{-2} min at 950 °C, Fig. 14, which correlates with the grain growth shown in Fig. 4.

The main challenge of the dual- and multiphase materials design is maximizing the ionic conducting volume without losing too much electronic conduction determined by the electronic conductivity of the selected phases as well as continuous percolation paths for the transport. While percolation is considering solely the volume fractions, the "contiguity" was introduced in[71,72] additionally accounting for the grain sizes of the individual phases. It can be expressed as the fraction of the total interconnected surface area of one phase shared with particles of the same phase and helps to estimate percolation and conducting properties within the dual-phase OTM composite.[73] Therefore, the contiguity of both the ionic conducting phase as well as the sum of electronic conducting phases was determined and shown in Fig. 14.

$$C_i + C_e = 1$$

$$V_i + V_e = 1$$

$$C_i = \frac{V_i \times R}{V_i \times R + V_e}$$

with $R = \frac{d_e}{d_i}$, V_i and V_e are the volume fraction of the ionic- and electron-conducting phases, respectively.

Indeed, the contiguity of electron conducting phase for the short dwell times is lower compared to higher dwell times, Fig. 14, which might be due to not fully sintered phases. However, it cannot explain the high permeance after 100 hours sintering, where the contiguity remains stable compared to 1–5 hours sintering.

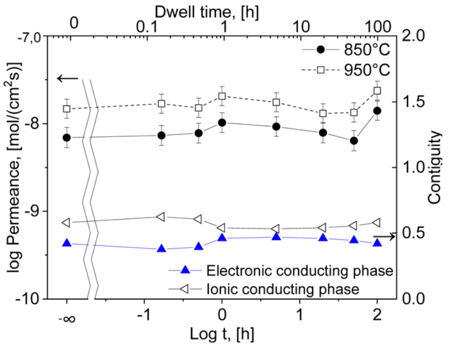

Fig. 14 Permeation and contiguity of the phases in the 60CGO20–FCO composite sintered at 1200 °C with activation energy of the permeation depending on the dwell time (solid lines are a guide to the eye).

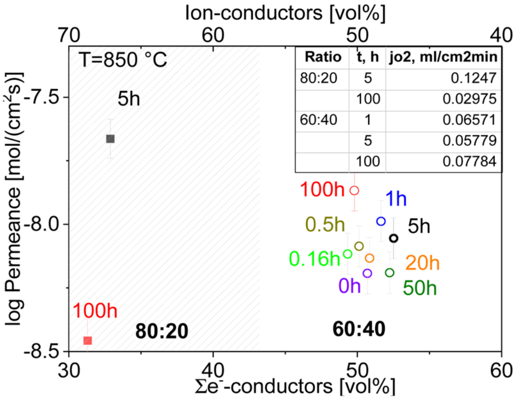

Ratio	t, h	jo2, ml/cm2min
80:20	5	0.1247
	100	0.02975
60:40	1	0.06571
	5	0.05779
	100	0.07784

Fig. 15 Comparison of the final permeation performance permeance of CGO20–FCO composite with ratio 60 : 40 and 80 : 20 sintered with various dwell times depending on the volume fraction of e$^-$-conducting phases.

The permeation of all composites at 850 °C with respect to the electron-conducting phase volume fraction is shown in Fig. 15. Among the various dwell times, the best results are found for the 100-h sintered sample of 60 : 40 ratio, which shows a stable dense microstructure with large grains and a low level of porosity. The large grain size is favourable in this case because less grain boundaries are involved, which typically act as barrier for the transport of charged carriers in particular ions.[13]

Although the oxygen permeance of the 100 h fired sample is the best among the differently sintered multiphase 60CGO20–FCO samples, comparison of the performance with other composite variations[14] shows the importance of the microstructure design. In general, the oxygen flux comparison of 60 : 40 with 80 : 20 fluorite: spinel weight ratio (Fig. 16) sintered at 1200 °C for 5 hours shows, that the reduction of the electron conducting phase volume effectively helps to improve permeation performance, reaching maximum j_{O_2} = 0.12 and 0.22 mL cm^{-2} min for the 80 wt% CGO20 in composite with fine grain size at 850 °C and 1000 °C respectively.

Interestingly, the 80CGO20–FCO fired for 100 hours showed a drastic drop in the oxygen flux. While in a 60 : 40 ratio, the amount of e-conducting phase is sufficient to provide continuous paths, regardless of the grain size, in 80 : 20 the large grains with a size of approx. 1.1 μm possibly lead to the insulation of the electron-conducting phase. Obviously, the coarser microstructure leads to lower electronic contiguity and overall percolation. In this case, the lower number of grain boundaries plays only a minor role.

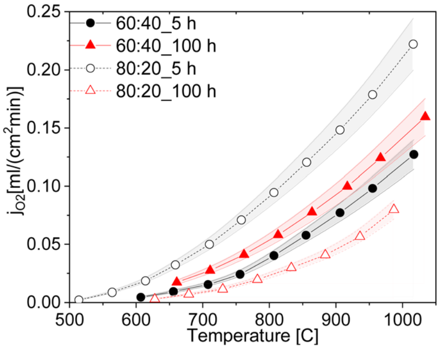

Fig. 16 Oxygen permeation rates of the ceria-based materials with 60 : 40 and 80 : 20 ratios sintered at 5 and 100 h (solid lines are a guide to the eye).

4. Conclusions

Dual-phase dense 60 wt% $Ce_{0.8}Gd_{0.2}O_{2-\delta}$–40 wt% $FeCo_2O_4$ membranes were successfully synthesized by solid-state reactive sintering with one-step thermal processing at 1200 °C using commercially available $Ce_{0.8}Gd_{0.2}O_{2-\delta}$, Co_3O_4 and Fe_2O_3 as raw materials. The influence of the sintering parameters was systematically studied by varying the dwelling time and cooling methods.

It was found that already at 0 h dwell time, the phase interaction was completed, and all phases were present: fluorite, spinel, and perovskite. All samples sintered <1 h dwell time, however, reveal insufficient densification, *i.e.*, a high porosity and not connected matrix of the phases. That emphasizes that a longer dwell time is required to obtain a close-packed and uniformly distributed microstructure. The 100 hours sintered sample shows the best permeation performance with j_{O_2} = 0.078 mL cm^{-2} min at 850 °C thanks to the improved microstructure with enlarged grains. However, the implementation of such conditions is not reasonable for future scale-up towards potential commercialization, due to very long dwell time. Although the 80 : 20 composite sintered for 100 h has a similar grain size, its performance is very poor. Apparently, the isolation of the minor phase (electron-conducting phase) occurs, which negatively affects the percolation and hence oxygen flux. Close to the percolation limit grain and pore size as well as porosity level are very important features in the microstructural design of composite membranes.

The influence of the sintering profile on the microstructural features such as grain size distribution, pore volume and size, as well as density were discussed. The initial mix of the oxides undergoes some modification during the sintering process and results in a multi-phase microstructure with coexistence of fluorite, perovskite, and two spinel types, except the 100 hours fired pellets, where an additional high-temperature CoO phase is observed. The grain growth as well as pore growth are dependent on the dwell time. The mean grain size increased moderately from 0.57–0.77 μm between 1 and 50 hours dwell time and reached its maximum of 1.13 μm in a 100 h fired sample. The relative density maximum of 93 and 94% were obtained for the 5 and 100 h sintered samples. The de-densification phenomenon is observed for the 20 and 50-h sintered samples, where intensive grain and pore growth occurs simultaneously.

TEM analysis indicated a few CoO grains located next to Co_3O_4 spinel grains in the 100 h fired sample. In this case, residual high-temperature CoO is identified due to the long dwell time, where a higher amount of CoO is formed and does not have enough time to re-oxidize during cooling completely. The control of the cooling rate can thus govern the process of the Co rearranging between the Co_3O_4 and CoO phases until the equilibrium is reached. Moreover, it was observed that slow cooling with an additional step for 100 hours at 850 °C helps to eliminate the CoO phase and preserve the desired fluorite, spinel, and perovskite phase mixture. This emphasizes the importance of the slow cooling for the Fe–Co spinel within our composite system.

Among all chosen conditions, the intermediate time of 5 hours at 1200 °C sintering temperature is the most suitable for the CGO20–FCO multi-phase composite showing good structure-related properties with optimised grain size and low porosity and oxygen permeation with oxygen flux of j_{O_2} = 0.06 mL cm^{-2} min at 850 °C. Moreover, a cooling rate of 0.5 K min^{-1} between 900 and 800 °C is sufficient to re-oxidize the CoO phase to get the desired spinel structure. Future study of the stability and durability in application-oriented conditions is required in order to exploit such complex composite materials.

Author contributions

Liudmila Fischer: investigation & writing – original draft preparation; Ke Ran: investigation & writing – original draft preparation, Doris Sebold: investigation, Patrick Behr: investigation, Stefan Baumann: conceptualization, investigation, funding acquisition & writing – original draft, Joachim Mayer: funding acquisition, & writing – review & editing, Arian Nijmeijer: supervision & writing – review & editing, Henny J.M. Bouwmeester: conceptualization, Oliver Guillon resources, supervision & writing – review & editinZg; Wilhelm A. Meulenberg: resources, supervision & writing – review & editing.

Conflicts of interest

There are no conflicts to declare.

Acknowledgements

The work is funded by the Deutsche Forschungsgemeinschaft (DFG, German Research Foundation) – 387282673. Ke Ran acknowledges support by the Bundesministerium für Bildung und Forschung (NEUROTEC, 16ME0399, and 16ME0398K). We would like to thank Mr S. Heinz for the assistances in lab works, sample preparations and permeation measurements.

Notes and references

1 J. Sunarso, S. Baumann, J. M. Serra, W. A. Meulenberg, S. Liu, Y. S. Lin and J. C. Diniz da Costa, *J. Membr. Sci.*, 2008, **320**, 13.
2 R. Kiebach, S. Pirou, L. Martinez Aguilera, A. B. Haugen, A. Kaiser, P. V. Hendriksen, M. Balaguer, J. García-Fayos, J. M. Serra, F. Schulze-Küppers, M. Christie, L. Fischer, W. A. Meulenberg and S. Baumann, *J. Mater. Chem. A*, 2022, **10**, 2152.
3 G. Chen, A. Feldhoff, A. Weidenkaff, C. Li, S. Liu, X. Zhu, J. Sunarso, K. Huang, X.-Y. Wu, A. F. Ghoniem, W. Yang, J. Xue, H. Wang, Z. Shao, J. H. Duffy, K. S. Brinkman, X. Tan, Y. Zhang, H. Jiang, R. Costa, K. A. Friedrich and R. Kriegel, *Adv. Funct. Mater.*, 2022, **32**, 2105702.
4 W. Bai, J. Feng, C. Luo, P. Zhang, H. Wang, Y. Yang, Y. Zhao and H. Fan, *Int. J. Hydrogen Energy*, 2021, **46**, 36257.
5 J. Zhao, Y. Pang, C. Su, S. Jiang and L. Ge, *Energy Fuels*, 2023, **37**, 7042.
6 A. Leo, S. Liu and J. C. Diniz da Costa, *Int. J. Greenhouse Gas Control*, 2009, **3**, 357.
7 S. Smart, C. X. C. Lin, L. Ding, K. Thambimuthu and J. C. Diniz da Costa, *Energy Environ. Sci.*, 2010, **3**, 268.
8 M. Balaguer, J. García-Fayos, C. Solís and J. M. Serra, *Chem. Mater.*, 2013, **25**, 4986.
9 J. Garcia-Fayos, M. Balaguer, S. Baumann and J. M. Serra, *J. Membr. Sci.*, 2018, **548**, 117.
10 H. Takamura, K. Okumura, Y. Koshino, A. Kamegawa and M. Okada, *J. Electroceram.*, 2004, **13**, 613.
11 M. Ramasamy, *Dual Phase Oxygen Transport Membrane for Efficient Oxyfuel Combustion*, Forschungszentrum Jülich GmbH, Jülich, 2016.
12 W. Fang, F. Liang, Z. Cao, F. Steinbach and A. Feldhoff, *Angew. Chem., Int. Ed.*, 2015, **54**, 4847.
13 Y. Lin, S. Fang, D. Su, K. S. Brinkman and F. Chen, *Nat. Commun.*, 2015, **6**, 6824.
14 L. Fischer, K. Neuhaus, C. Schmidt, K. Ran, P. Behr, S. Baumann, J. Mayer and W. A. Meulenberg, *J. Mater. Chem. A*, 2022, **10**, 2412.
15 F. Zeng, S. Baumann, J. Malzbender, A. Nijmeijer, L. Winnubst, O. Guillon, R. Schwaiger and W. A. Meulenberg, *J. Membr. Sci.*, 2021, **628**, 119248.
16 A. Arratibel Plazaola, A. Cruellas Labella, Y. Liu, N. Badiola Porras, D. Pacheco Tanaka, M. Sint Annaland and F. Gallucci, *Processes*, 2019, **7**, 128.
17 M. Coduri, S. Checchia, M. Longhi, D. Ceresoli and M. Scavini, *Front. Chem.*, 2018, **6**, 526.
18 J. H. Joo, K. S. Yun, Y. Lee, J. Jung, C.-Y. Yoo and J. H. Yu, *Chem. Mater.*, 2014, **26**, 4387.
19 S. Presto, C. Artini, M. Pani, M. M. Carnasciali, S. Massardo and M. Viviani, *Phys. Chem. Chem. Phys.*, 2018, **20**, 28338.
20 J. A. Kilner and M. Burriel, *Annu. Rev. Mater. Res.*, 2014, **44**, 365.
21 J. Koettgen, S. Grieshammer, P. Hein, B. O. H. Grope, M. Nakayama and M. Martin, *Phys. Chem. Chem. Phys.*, 2018, **20**, 14291.
22 T. Kiefer, *Entwicklung neuer Schutz- und Kontaktierungsschichten für Hochtemperatur-Brennstoffzellen*, Forschungszentrum, Zentralbibliothek, Jülich 2008.
23 A. J. Samson, M. Søgaard and P. Vang Hendriksen, *J. Membr. Sci.*, 2014, **470**, 178.
24 N. Bahlawane, P. H. T. Ngamou, V. Vannier, T. Kottke, J. Heberle and K. Kohse-Höinghaus, *Phys. Chem. Chem. Phys.*, 2009, **11**, 9224.

25 M. Ramasamy, E. S. Persoon, S. Baumann, M. Schroeder, F. Schulze-Küppers, D. Görtz, R. Bhave, M. Bram and W. A. Meulenberg, *J. Membr. Sci.*, 2017, **544**, 278.

26 L. Fischer, K. Ran, C. Schmidt, K. Neuhaus, S. Baumann, P. Behr, J. Mayer, H. J. M. Bouwmeester, A. Nijmeijer, O. Guillon and W. A. Meulenberg, *Membranes*, 2023, 13.

27 L. Fischer, K. Ran, C. Schmidt, K. Neuhaus, S. Baumann, P. Behr, J. Mayer, H. J. Bouwmeester, A. Nijmeijer, O. Guillon and W. A. Meulenberg, *Open Ceram.*, 2024, **17**, 100519.

28 X. Zhu and W. Yang, *AIChE J.*, 2008, **54**, 665.

29 C. D. Lorenz and R. M. Ziff, *J. Chem. Phys.*, 2001, **114**, 3659.

30 M. Ge, X. Huang, H. Yan, D. Gursoy, Y. Meng, J. Zhang, S. Ghose, W. K. S. Chiu, K. S. Brinkman and Y. S. Chu, *Commun. Mater.*, 2022, 3.

31 Z. Zhang, W. Zhou, Y. Chen, D. Chen, J. Chen, S. Liu, W. Jin and Z. Shao, *ACS Appl. Mater. Interfaces*, 2015, **7**, 22918.

32 K. Ran, F. Zeng, L. Fischer, S. Baumann, W. A. Meulenberg, K. Neuhaus and J. Mayer, *Acta Mater.*, 2022, **234**, 118034.

33 K. Yasuda, K. Uemura and T. Shiota, *J. Phys.: Conf. Ser.*, 2012, **339**, 12006.

34 K. Raju, S. Kim, C. J. Hyung, J. H. Yu, Y.-H. Seong, S.-H. Kim and I.-S. Han, *Ceram. Int.*, 2019, **45**, 1460.

35 J. H. Joo, G. S. Park, C.-Y. Yoo and J. H. Yu, *Solid State Ionics*, 2013, **253**, 64.

36 Q. Li, X. Zhu, Y. He, Y. Cong and W. Yang, *J. Membr. Sci.*, 2011, **367**, 134.

37 V. V. Kharton, *Solid State Ionics*, 2003, **160**, 247.

38 H. Luo, H. Jiang, K. Efimov, F. Liang, H. Wang and J. Caro, *Ind. Eng. Chem. Res.*, 2011, **50**, 13508.

39 J.-L. Shi, Y. Deguchi and Y. Sakabe, *J. Mater. Sci.*, 2005, **40**, 5711.

40 K.-T. Lee, D.-K. Kim, J.-H. Park and I.-J. Shon, *Ceram. Int.*, 2009, **35**, 1345.

41 T. Zhang, P. Hing, H. Huang and J. Kilner, *J. Eur. Ceram. Soc.*, 2002, **22**, 27.

42 V. Gil, J. Tartaj, C. Moure and P. Durán, *J. Eur. Ceram. Soc.*, 2006, **26**, 3161.

43 T. Zhang, P. Hing, H. Huang and J. Kilner, *J. Eur. Ceram. Soc.*, 2001, **21**, 2221.

44 E. Jud, C. B. Huwiler and L. J. Gauckler, *Nippon Seramikkusu Kyokai gakujutsu ronbunshi*, 2006, **114**, 963.

45 F. Zeng, J. Malzbender, S. Baumann, A. Nijmeijer, L. Winnubst, M. Ziegner, O. Guillon, R. Schwaiger and W. A. Meulenberg, *J. Eur. Ceram. Soc.*, 2021, **41**, 509.

46 P. J. Murray and J. W. Linnett, *J. Phys. Chem. Solids*, 1976, **37**, 619.

47 A. N. Hansson, S. Linderoth, M. Mogensen and M. A. Somers, *J. Alloys Compd.*, 2005, **402**, 194.

48 T. W. Ridler and S. Calvard, *IEEE Trans. Syst. Man Cybern.*, 1978, **8**, 630.

49 A. Kovács, R. Schierholz and K. Tillmann, *J. Large Scale Res. Facil.*, 2016, 2.

50 F. Zeng, J. Malzbender, S. Baumann, W. Zhou, M. Ziegner, A. Nijmeijer, O. Guillon, R. Schwaiger and W. Albert Meulenberg, *J. Am. Ceram. Soc.*, 2021, **104**, 1814.

51 T. Ferreira, J. C. Waerenborgh, M. Mendonça, M. R. Nunes and F. M. Costa, *Solid State Sci.*, 2003, **5**, 383.

52 M. G. Brik, A. Suchocki and A. Kamińska, *Inorg. Chem.*, 2014, **53**, 5088.

53 Y. Ji, J. Kilner and M. Carolan, *J. Eur. Ceram. Soc.*, 2004, **24**, 3613.

54 V. V. Kharton, F. M. Figueiredo, L. Navarro, E. N. Naumovich, A. V. Kovalevsky, A. A. Yaremchenko, A. P. Viskup, A. Carneiro, F. M. B. Marques and J. R. Frade, *J. Mater. Sci.*, 2001, **36**, 1105.

55 C. Artini, M. Pani, M. M. Carnasciali, J. R. Plaisier and G. A. Costa, *Inorg. Chem.*, 2016, **55**, 10567.

56 F. Zeng, *Mechanical reliability and oxygen permeation of* $Ce_{0.8}Gd_{0.2}O_{2-\delta}$–$FeCo_2O_4$ dual-phase composite, University of Twente, Enschede, 2021.

57 S. J. Hong and A. V. Virkar, *J. Am. Ceram. Soc.*, 1995, **78**, 433.

58 M. N. Rahaman, *Ceramic Processing and Sintering*, CRC Press, 2017.

59 C. A. Schneider, W. S. Rasband and K. W. Eliceiri, *Nat. Methods*, 2012, **9**, 671.

60 B. Stawarczyk, M. Ozcan, L. Hallmann, A. Ender, A. Mehl and C. H. F. Hämmerlet, *Clin. oral investig.*, 2013, **17**, 269.

61 D. Pérez-Coll, E. Sánchez-López and G. C. Mather, *Solid State Ionics*, 2010, **181**, 1033.

62 J. L. Shi, *J. Mater. Res.*, 1999, **14**, 1389.

63 F. Schulze-Küppers, S. Baumann, F. Tietz, H. Bouwmeester and W. A. Meulenberg, *J. Eur. Ceram. Soc.*, 2014, **34**, 3741.

64 X. Chen, H. van Gog and M. A. van Huis, *J. Mater. Chem. C*, 2021, **9**, 5662.

65 F.-C. Kong, Y.-F. Li, C. Shang and Z.-P. Liu, *J. Phys. Chem. C*, 2019, **123**, 17539.

66 F. Zeng, S. Baumann, J. Malzbender, A. Nijmeijer, L. Winnubst, O. Guillon, R. Schwaiger and W. A. Meulenberg, *J. Membr. Sci.*, 2021, **628**, 119248.

67 M. Żyła, G. Smoła, A. Knapik, J. Rysz, M. Sitarz and Z. Grzesik, *Corros. Sci.*, 2016, **112**, 536.

68 A. Kaczmarska, Z. Grzesik and S. Mrowec, *High Temp. Mater. Processes*, 2012, **31**, 371.

69 L. Fuhsing, S. Tinkler and R. Diekmann, *Solid State Ionics*, 1993, **62**, 39.

70 V. V. Kharton, A. L. Shaula, E. N. Naumovich, N. P. Vyshatko, I. P. Marozau, A. P. Viskup and F. M. B. Marques, *J. Electrochem. Soc.*, 2003, **150**, J33.

71 J. Gurland, Brown University, Division of Engineering, United States, Office of Ordnance Research, *The Measurement of Grain Contiguity in Two-phase Alloys*, Division of Engineering, Brown University, 1957.

72 Z. Fan, A. P. Miodownik and P. Tsakiropoulos, *Mater. Sci. Technol.*, 1993, **9**, 1094.

73 F. Zeng, J. Malzbender, S. Baumann, M. Krüger, L. Winnubst, O. Guillon and W. A. Meulenberg, *J. Eur. Ceram. Soc.*, 2020, **40**, 5646.